Amplitude Analysis of Single-Wavelength Time-Dependent Absorption Data Does Not Support the Conventional Sequential Mechanism for the Reduction of Dioxygen to Water Catalyzed by Bovine Heart Cytochrome *c* Oxidase†

Istvan Szundi, Jenny Cappuccio, and Ólöf Einarsdóttir*

Department of Chemistry and Biochemistry, University of California, Santa Cruz, California 95064

Received March 26, 2004; Revised Manuscript Received August 31, 2004

ABSTRACT: The reactions of fully reduced and mixed-valence bovine heart cytochrome *c* oxidase with dioxygen have been reinvestigated in the absence and presence of metal ions (Zn^{2+}, Ni^{2+}, and Cd^{2+}) by time-resolved optical absorption spectroscopy using the CO flow-flash technique. The time-resolved data were recorded on a microsecond to millisecond time scale at 442, 610, and 820 nm and subjected to quantitative amplitude analysis based on a conventional unidirectional sequential mechanism. The amplitudes of the sequential intermediates are derived from the absorbance changes associated with the different exponentials and from the kinetic equations of the sequential scheme. The general relationship between the pre-exponential factors and the absorbance of the successive intermediates in the sequential scheme is presented. A comparison of the experimental amplitudes of the individual intermediates with the model amplitudes at the three wavelengths indicates that the low spin heme *a* is incompletely oxidized during the formation of the sequential $\mathbf{P_R}$ intermediate ($\mathbf{P_{R,s}}$). The conversion of the sequential **F** intermediate to the oxidized enzyme occurs on two millisecond time scales. The amplitude analysis of the single-wavelength data does not support the conventional sequential mechanism for the reduction of dioxygen to water catalyzed by cytochrome *c* oxidase.

Cytochrome oxidase catalyzes the reduction of dioxygen to water and couples this reaction to the transfer of protons across the mitochondrial or bacterial membrane (*1*). This generates an electrochemical proton gradient, which is used to drive ATP synthesis by ATP synthase (for reviews, see refs *2*−*4*).

It is generally believed that the reduction of dioxygen to water by fully reduced cytochrome *c* oxidase involves five intermediates: the reduced enzyme ($\mathbf{R_s}$),[1] the dioxygen-bound form, $\mathbf{A_{R,s}}$ (compound **A**), the so-called "peroxy" form ($\mathbf{P_{R,s}}$), the oxy−ferryl form ($\mathbf{F_s}$), and the oxidized form ($\mathbf{O_s}$) (*2*, *3*, *5*). The subscript **s** refers to intermediates that are derived using the conventional sequential scheme, and which may or may not consist of a single chemical structure (species) with unique spectral features. In the conventional unidirectional sequential mechanism, these intermediates are generally connected via irreversible steps, although the binding of dioxygen to the reduced enzyme has been reported to be reversible (*3*, *6*−*10*). Transient optical absorption measurements have provided information about the kinetics of the electron and proton transfer steps (*7*, *9*, *11*−*16*), while time-resolved resonance Raman experiments have yielded useful information about the structures of the intermediates (*8*, *17*−*20*). Low-temperature optical absorption studies (*21*, *22*) and EPR measurements (*23*−*25*) have also provided important information about some of the transient intermediates.

Proton uptake studies have shown that two of the four scalar protons necessary for converting dioxygen to water are taken up with the rates of the $\mathbf{P_{R,s}}$-to-$\mathbf{F_s}$ and $\mathbf{F_s}$-to-$\mathbf{O_s}$ transitions (*26*−*29*). The other two protons most likely arise from internal proton donors in the reduced enzyme, which are protonated during the reduction of the oxidized enzyme (*30*, *31*). Two proton channels, the D-pathway and the K-pathway, have been identified in heme−copper oxidases (*32*−*34*). The D-pathway has been proposed to be respon-

† This work was supported by National Institutes of Health Grant GM 53788.

* To whom correspondence should be addressed. Fax: (831) 459-2935. Phone: (831) 459-3155. E-mail: olof@chemistry.ucsc.edu.

[1] Abbreviations: a^{3+}, oxidized low-spin heme *a*; a^{2+}, reduced low-spin heme *a*; a_3^{3+}, oxidized high-spin heme a_3; a_3^{2+}, reduced high-spin heme a_3; Cu_A, binuclear mixed-valence copper A center; Cu_B, copper B; *a*, low-spin heme *a*; a_3, heme a_3; $\mathbf{R_s}$, fully reduced cytochrome oxidase intermediate postulated by the conventional sequential mechanism; $\mathbf{R_M}$, mixed-valence cytochrome *c* oxidase, with the binuclear center reduced and heme *a* and Cu_A oxidized; compound **A**, ferrous−dioxygen complex of heme a_3; $\mathbf{A_M}$, compound **A** of the mixed-valence enzyme; $\mathbf{A_{R,s}}$, dioxygen-bound ferrous heme a_3 intermediate postulated by the conventional sequential mechanism; **P**, "peroxy" form of the enzyme generated on the bench in which heme a_3 has an absorption maximum at ∼607 nm when referenced against its oxidized state; $\mathbf{P_M}$, "peroxy" intermediate [a_3^{4+}═O^{2-} Cu_B^{2+}−OH^- (TyrO•) a^{3+} Cu_A^{2+}] formed at the binuclear center during the reaction of the mixed-valence enzyme with dioxygen; $\mathbf{P_{R,s}}$, "peroxy" intermediate postulated by the conventional sequential mechanism; $\mathbf{P_R}$, species with a redox state [a_3^{4+}═O^{2-} Cu_B^{2+}−OH^- ($TyrO^-$) a^{3+} Cu_A^+] and a spectrum equivalent to that of $\mathbf{P_M}$, corrected for the redox state of Cu_A; **F**, oxy−ferryl form of the enzyme generated on the bench in which heme a_3 has an absorption maximum at ∼580 nm when referenced against its oxidized state; $\mathbf{F_I}$, **F** in which heme *a* is oxidized and Cu_A is reduced; $\mathbf{F_{II}}$, **F** in which heme *a* is reduced and Cu_A is oxidized; $\mathbf{O_s}$, oxidized intermediate postulated by the conventional sequential mechanism; $\mathbf{F_s}$, oxy−ferryl intermediate postulated by the conventional sequential mechanism; SVD, singular-value decomposition; *b* value, pre-exponential factor which represents the absorbance amplitude associated with a respective first-order process.

10.1021/bi049408p CCC: $27.50
Published on Web 11/20/2004

sible for the uptake of both scalar and translocated protons during the oxidation of the enzyme by dioxygen (*35*−*37*), while proton uptake during the reduction of the oxidized enzyme has been associated with the K-pathway (*35*, *38*−*40*).

Additional insight into the role of the proton transfer pathways can be obtained by inhibiting proton uptake through either of these pathways. Zn^{2+} inhibition of bovine heart cytochrome *c* oxidase reconstituted into liposomes (*41*) and reconstituted *Escherichia coli* bo_3 oxidase (*42*) has been reported, and Zn^{2+} was recently shown to uncouple electron transfer and proton translocation in reconstituted cytochrome oxidase from *Paracoccus denitrificans* (*43*). Mills and coworkers also found the reconstituted *Rhodobacter sphaeroides* enzyme to be strongly inhibited by Zn^{2+} in the presence of a membrane potential (*44*).

Zinc ions have recently been shown to inhibit the oxidation of isolated *R. sphaeroides* cytochrome oxidase by dioxygen (*45*, *46*). While the rates of the formation and decay of the $\mathbf{F_s}$ intermediate in the flow-flash experiments were decreased by a factor of approximately 2 or 3 in the presence of Zn^{2+}, proton uptake through the D-pathway during $\mathbf{F_s}$ formation was found to be slowed by a factor of >20 (*46*). Zn^{2+} has also been shown to reversibly inhibit proton uptake in several membrane-bound enzymes, including bacterial photosynthetic reaction centers (*47*−*49*), the bc_1 complex (*47*, *50*), and voltage-gated proton channels (*51*).

The molecular interpretation of previous transient optical absorption data in terms of the coupling between electron transfer and proton uptake through the two proton pathways in cytochrome *c* oxidase has generally been based on the conventional sequential scheme. The sequence and kinetics of individual steps are primarily derived from multiexponential fits to time-dependent absorption data recorded at single wavelengths during the oxidation of the reduced enzyme by dioxygen and from the assignment of a few characteristic absorbance changes to specific intermediates (*7*, *9*, *12*, *13*). Intermediate absorbance amplitudes have also been estimated from the simulation of the absorbance changes occurring when the reduced enzyme reacts with dioxygen (*9*). However, there has been no direct calculation of the amplitudes of the sequential intermediates based on the results of the multiexponential fits, which would allow a straightforward testing of the unidirectional sequential scheme.

Recently, we questioned the general validity of the unidirectional sequential mechanism based on discrepancies observed at different pH values between the spectral shapes of the experimental $\mathbf{P_{R,s}}$ intermediate and the postulated model spectrum, generated by exposing the oxidized enzyme to a mixture of CO and O_2 (*52*, *53*). The latter is identical to that of $\mathbf{P_M}$ formed during the reaction of the mixed-valence enzyme with dioxygen (*54*). In particular, some of the steps proposed in our alternative mechanism (*52*, *53*) may involve internal proton transfer, which could be influenced by the presence of Zn^{2+} and other ions, thus leading to more pronounced deviations in the kinetics from the conventional sequential model.

In this study, we reinvestigated the oxidation of cytochrome oxidase by dioxygen in the absence and presence of metal ions. We used single-wavelength detection in combination with a quantitative derivation of absorbance amplitudes. Kinetic analysis of the data in terms of a conventional sequential mechanism and calculation of the amplitudes of individual intermediates at different wavelengths are presented. A comparison of the experimental amplitudes of the individual intermediates at three different wavelengths with the model amplitudes indicates that the oxidation of the low-spin heme *a* both in the presence and in the absence of metal ions is incomplete during the formation of $\mathbf{P_{R,s}}$ and also occurs on a 100−200 μs time scale. The conversion of $\mathbf{F_s}$ to the oxidized enzyme occurs on two millisecond time scales. We show that the sequential model can be tested and evaluated quantitatively using concepts from a traditional kinetic approach.

MATERIALS AND METHODS

Sample Preparation. Cytochrome *c* oxidase was isolated from bovine hearts according to the method of Yoshikawa et al. (*55*) with a minor modification. The first cholate precipitation was increased from 3.2 to 3.8%, and the subsequent ammonium sulfate fractionations were at 33 and 60%. The relevant spectroscopic ratios were as follows: $A_{444(red)}/A_{420(ox)} = 1.3$, $A_{444(red)}/A_{420(red)} = 2.3$, and $A_{604(red)}/A_{598(ox)} = 2.2$. The final precipitate was dissolved in 50 mM HEPES-KOH (pH 7.5) and 0.1% β-D-dodecyl maltoside and dialyzed against the same buffer overnight. To remove residual phosphate used during the isolation procedure, the enzyme solution was passed through a G-75 Sephadex column, equilibrated in 50 mM HEPES-KOH (pH 7.5) and 0.1% β-D-dodecyl maltoside. The enzyme solution was subsequently passed through a CM-Sepharose cationic exchange column, equilibrated in the same buffer, to eliminate any residual metal ions. The reduced enzyme was formed by the addition of sodium ascorbate and ruthenium hexammine to an anaerobic solution of the oxidized enzyme. Subsequent exposure to CO formed the reduced CO-bound enzyme. The cytochrome oxidase concentration, which equals half the heme A concentration, was determined spectrophotometrically using extinction coefficients of 159.2 mM^{-1} cm^{-1} at 420 nm for the fully oxidized enzyme and 212.8 mM^{-1} cm^{-1} at 444 nm for the reduced enzyme (*56*).

Absorption Measurements. The reaction of the fully reduced enzyme with dioxygen was carried out using the flow-flash method (*57*, *58*) as previously described (*59*). The reaction was monitored in the absence of metal ions and in the presence of 300 μM Zn^{2+}, Cd^{2+}, and Ni^{2+} at pH 7.5. Briefly, the fully reduced CO-bound enzyme was mixed with O_2-saturated buffer in a 1:1 ratio in a 10 μL flow cell interfaced with a laser photolysis system. The reaction of the reduced enzyme with dioxygen was monitored at 442, 610, and 820 nm using a tungsten lamp. Interference filters at 442 and 610 nm and a 650 nm high-pass filter were used to restrict the probe light passing through the sample to the appropriate wavelength. The transmitted beam was passed through a monochromator and a matching interference or cutoff filter to reduce the signal from laser scattering. The signals were detected by a photodiode at 820 nm and a photomultiplier at 610 and 442 nm, and were recorded with a 500 MHz digital oscilloscope (Le Croy 9350AM). Each kinetic trace was an average of 40 scans. The laser artifacts, which decayed with the instrument response time (1.3 μs for the photodiode and 2.1 μs for the photomultiplier), were removed from the signals by deconvolution or by a simple

exponential fitting to the early microsecond time points. The time-dependent signals were converted to a logarithmic time scale. Each decade in the logarithmic time window was divided into 100 segments, and the data points in each segment were averaged to give a single point. The corrected absorbance traces were fitted globally to a sum of exponentials. The earliest time points (<10 μs) were smoothed and weighted when it was required for increased accuracy of the fit to the rest of the curve. The fitting and all other calculations were carried out with programs written in Matlab (The Mathworks, Inc.).

The model spectra of the individual intermediates are linear combinations of ground-state spectra of the oxidized, reduced, mixed-valence CO, and fully reduced CO enzyme, the oxidized spectrum of Cu_A (*60*), and the spectra of **P** and **F**, prepared as previously described (*61*).

Calculation of the Amplitudes of the Sequential Intermediates. The analysis of the reaction kinetics presented here is based on the assumption of first-order kinetics, where the time-dependent concentration of intermediates can be described by a sum of exponential functions:

$$A(t) = b_1 \exp(-k_1 t) + b_2 \exp(-k_2 t) + b_3 \exp(-k_3 t) + ... + b_0 \quad (1)$$

Neither the apparent rate k_i nor the kinetic amplitude b_i in the exponential fit has a direct physical meaning, but both are mathematical abstractions. To convert them into microscopic rate constants and intermediate absorbances, we must propose a reaction scheme. Below we describe the theoretical treatment of unidirectional sequential schemes using a four-intermediate sequence:

$$\mathrm{K} \xrightarrow{k_1} \mathrm{L} \xrightarrow{k_2} \mathrm{M} \xrightarrow{k_3} \mathrm{N}$$

The time-dependent change in the intermediate concentrations can be described by a set of linear first-order differential equations:

$$-\mathrm{d[K]}/\mathrm{d}t = k_1[\mathrm{K}]; \; -\mathrm{d[L]}/\mathrm{d}t = k_2[\mathrm{L}] - k_1[\mathrm{K}];$$
$$-\mathrm{d[M]}/\mathrm{d}t = k_3[\mathrm{M}] - k_2[\mathrm{L}]; \; -\mathrm{d[N]}/\mathrm{d}t = -k_3[\mathrm{M}]$$

Solving the differential equations provides the time-dependent concentration of each intermediate as a sum of exponential functions:

$$[\mathrm{K}] = c_0 \exp(-k_1 t)$$

$$[\mathrm{L}] = c_0[-k_1/(k_1 - k_2) \exp(-k_1 t) + k_1/(k_1 - k_2) \exp(-k_2 t)]$$

$$[\mathrm{M}] = c_0[k_1 k_2/(k_1 - k_2)(k_1 - k_3) \exp(-k_1 t) - k_1 k_2/(k_1 - k_2)(k_2 - k_3) \exp(-k_2 t) + k_1 k_2/(k_1 - k_3)(k_2 - k_3) \exp(-k_3 t)]$$

$$[\mathrm{N}] = c_0[-k_2 k_3/(k_1 - k_2)(k_1 - k_3) \exp(-k_1 t) + k_1 k_3/(k_1 - k_2)(k_2 - k_3) \exp(-k_2 t) - k_1 k_2/(k_1 - k_3)(k_2 - k_3) \exp(-k_3 t) + 1]$$

The pre-exponential factors can be arranged in a matrix **W** (called the eigenvector matrix of the kinetic matrix in the algebraic method), where the first row contains the factors that appear in the expression for the first intermediate concentration [K], the second row those for the second intermediate concentration [L], etc.

$$\mathbf{W} = \begin{bmatrix} w_{11} & 0 & 0 & 0 \\ w_{21} & w_{22} & 0 & 0 \\ w_{31} & w_{32} & w_{33} & 0 \\ w_{41} & w_{42} & w_{43} & w_{41} \end{bmatrix}$$

where $w_{11} = w_{44} = c_0$, $w_{21} = -c_0 k_1/(k_1 - k_2)$, $w_{22} = c_0 k_1/(k_1 - k_2)$, $w_{31} = c_0 k_1 k_2/[(k_1 - k_2)(k_1 - k_3)]$, etc., as given by the known solution to the differential equations. c_0 is the initial concentration. Since $[\mathrm{K}(t = 0)] = [\mathrm{N}(t = \infty)] = c_0$ and $[\mathrm{L}(t = 0)] = [\mathrm{M}(t = 0)] = [\mathrm{N}(t = 0)] = [\mathrm{K}(t = \infty)] = [\mathrm{L}(t = \infty)] = [\mathrm{M}(t = \infty)] = 0$, the following relationships hold: $w_{21} + w_{22} = 0$, $w_{31} + w_{32} + w_{33} = 0$, $w_{41} + w_{42} + w_{43} + w_{44} = 0$. Note that each column of the **W** matrix contains the pre-exponential factors that belong to the same exponential in the time-dependent concentration functions for the different intermediates.

In practice, the time dependence is measured at a limited number of time points (n), and the time variable and the continuous functions of the concentrations should be replaced by a discrete time vector and a concentration vector of length n, respectively.

The four concentration vectors (**K**−**N**) of the intermediates can be arranged in a matrix form and can be represented as a product of two matrices:

$$\begin{bmatrix} \mathbf{K} \\ \mathbf{L} \\ \mathbf{M} \\ \mathbf{N} \end{bmatrix} = \begin{bmatrix} \mathbf{w}_{11} & 0 & 0 & 0 \\ \mathbf{w}_{21} & \mathbf{w}_{22} & 0 & 0 \\ \mathbf{w}_{31} & \mathbf{w}_{32} & \mathbf{w}_{33} & 0 \\ \mathbf{w}_{41} & \mathbf{w}_{42} & \mathbf{w}_{43} & \mathbf{w}_{44} \end{bmatrix} \times \begin{bmatrix} \exp(-\mathbf{k}_1 t) \\ \exp(-\mathbf{k}_2 t) \\ \exp(-\mathbf{k}_3 t) \\ \exp(-\mathbf{k}_4 t) \end{bmatrix}$$

$$\mathbf{C} \qquad \mathbf{W} \qquad \mathbf{T}$$

$$\mathbf{C} = \mathbf{W} \times \mathbf{T} \quad (2)$$

where **C** and **T** are $4 \times n$ matrices and **W** is a 4×4 matrix.

The intermediate concentrations cannot be measured directly. Instead, the total absorbance change, which includes contributions from each intermediate, is measured. The absorbance vector for our sequential kinetic model, $\mathbf{A}_{\mathrm{model}}$, can be written as a sum of four vectors:

$$\mathbf{A}_{\mathrm{model}} = \epsilon_{\mathrm{K}}\mathbf{K} + \epsilon_{\mathrm{L}}\mathbf{L} + \epsilon_{\mathrm{M}}\mathbf{M} + \epsilon_{\mathrm{N}}\mathbf{N} \quad (3)$$

where ϵ_{K}, ϵ_{L}, ϵ_{M}, and ϵ_{N} are the extinction coefficients of the four intermediates at the selected wavelength. These can be represented as a single-row matrix ($\boldsymbol{\epsilon} = [\epsilon_{\mathrm{K}}\ \epsilon_{\mathrm{L}}\ \epsilon_{\mathrm{M}}\ \epsilon_{\mathrm{N}}]$). On the basis of eq 2, $\mathbf{A}_{\mathrm{model}}$ can be written as

$$\mathbf{A}_{\mathrm{model}} = \boldsymbol{\epsilon} \times \mathbf{C} = \boldsymbol{\epsilon} \times \mathbf{W} \times \mathbf{T} \quad (4)$$

The experimentally observed time dependence of the absorbance at the particular wavelength, $\mathbf{A}_{\mathrm{exp}}$, is fitted to a sum of exponentials as already mentioned:

$$\mathbf{A}_{\mathrm{exp}} = b_1 \exp(-k_1 t) + b_2 \exp(-k_2 t) + b_3 \exp(-k_3 t) + b_0$$

This equation can be written in a matrix form as

$$\mathbf{A}_{\mathrm{exp}} = \mathbf{B} \times \mathbf{T} \quad (5)$$

where **B** is a row vector composed of the pre-exponential factors or *b* values ($[b_1\ b_2\ b_3\ b_0]$) and **T** is the familiar exponential time matrix. Comparing $\mathbf{A}_{model}$ (eq 4) with $\mathbf{A}_{exp}$ (eq 5), we find that the apparent rates from the multiexponential fits (eq 1) represent the microscopic rates in the scheme and the intermediate amplitudes (ϵ) are related to the kinetic amplitudes (*b* values):

$$\mathbf{B} = \epsilon \times \mathbf{W} \tag{6}$$

The exponential amplitudes from the experimental data (b_1, b_2, etc.) thus represent the sum of the absorbance contributions of the intermediates as given by the product of ϵ and **W** matrices. The intermediate amplitudes for the sequential scheme are calculated by carrying out a matrix inversion followed by a matrix multiplication, according to

$$\epsilon = \mathbf{B} \times \mathbf{W}^{-1} \tag{7}$$

For more complicated schemes, the analytical solution to the differential equations can be difficult to find, and the algebraic method for calculating intermediate amplitudes should be used.

RESULTS

Effect of Zn^{2+}, Cd^{2+}, and Ni^{2+} on the Reaction of the Fully Reduced Enzyme with Dioxygen. The oxidation of reduced cytochrome oxidase by dioxygen was monitored at 442, 610, and 820 nm following photolysis of the fully reduced CO-bound enzyme in the absence and presence of metal ions. Figure 1 shows transient kinetic traces at the three wavelengths in the absence of metal ions (blue) and in the presence of Zn^{2+} (red), Cd^{2+} (cyan), and Ni^{2+} (green). The data are displayed on a logarithmic time scale to better visualize individual processes. It is clear that all three metal ions affect the kinetics of cytochrome oxidase oxidation; the effects of Zn^{2+} and Cd^{2+} are similar, while the effect of Ni^{2+} is somewhat more pronounced.

In our analysis, we assume that the kinetics follow exponential behavior; nonexponential kinetics such as distributed kinetics, which require an entirely different and more sophisticated mathematical treatment, are not considered here. The kinetic traces in Figure 1 were fitted with an increasing number of exponentials. Figure 2 shows the transient data recorded in the absence (left panels, blue) and presence of Zn^{2+} (right panels, red), and the four-exponential (magenta) and five-exponential (green) fits to the data. The lifetimes from the four-exponential fit were 23 ± 4 μs, 35 ± 5 μs, 95 ± 10 μs, and 1.6 ± 0.2 ms in the absence of Zn^{2+} and 22 ± 4 μs, 43 ± 5 μs, 250 ± 20 μs, and 3.7 ± 0.2 ms in the presence of Zn^{2+}. The errors were estimated based on experiment-to-experiment variation rather than from error analysis of each data set. The lifetimes are in good agreement with previously reported values (*46*). The residuals (multiplied by a factor of 2 in Figure 2) from the four-exponential fit (magenta) clearly show significant structure on a millisecond time scale, which disappears when the data are fitted with an additional millisecond lifetime (green residual). The five lifetimes were 23 ± 4 μs, 38 ± 5 μs, 90 ± 10 μs, 1.2 ± 0.2 ms, and 3.9 ± 0.4 ms in the absence of Zn^{2+} and 22 ± 4 μs, 45 ± 5 μs, 190 ± 20 μs, 1.5 ± 0.2 ms, and 8.4 ± 1 ms in the presence of Zn^{2+}. Similar lifetimes were observed in the presence of Cd^{2+} and Ni^{2+}.

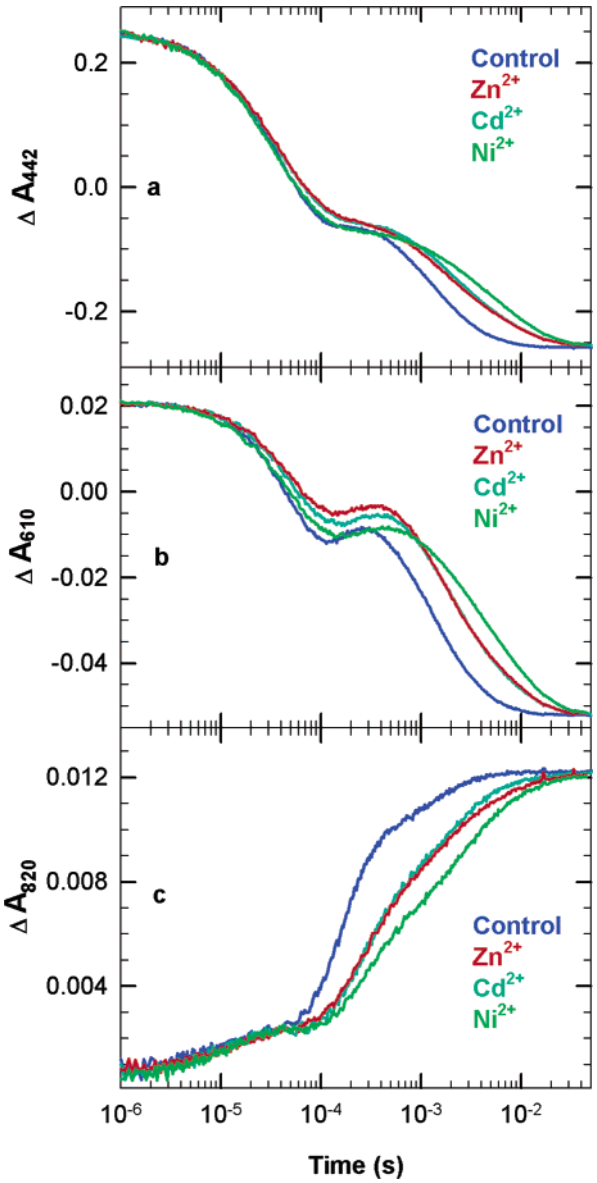

FIGURE 1: Transient absorbance changes taking place during the reduction of dioxygen to water following photolysis of the fully reduced CO-bound complex at (a) 442, (b) 610, and (c) 820 nm. The absorbance changes are normalized and displayed on a logarithmic time scale. The effective cytochrome oxidase concentration (after photolysis) was 4.1 μM, The reaction was carried out in 50 mM HEPES-KOH buffer (pH 7.4) and 0.1% β-D-dodecyl maltoside at 24 °C and was monitored in the absence of metals (blue, control) and the presence of 300 μM Zn^{2+} (red), Cd^{2+} (cyan), and Ni^{2+} (green). Each kinetic trace represents the average of 40 consecutive runs. The CO and O_2 concentrations after mixing were ~500 and 625 μM, respectively.

The lifetimes from the five-exponential fit in the absence and presence of the three metal ions are listed in Table 1. The shortest lifetime (~20 μs) may be slightly increased by the correction applied to remove the laser artifact. The 90 μs lifetime is increased by a factor of 2−3 in the presence of the metal ions, in agreement with previous studies by Brzezinski and co-workers (*45*, *46*). While the metal ions produced small but variable effects on the 1.2 ms lifetime, the second millisecond lifetime (~4 ms) is increased by a factor of 2 for all three metal ions. A lifetime of ~4 ms has

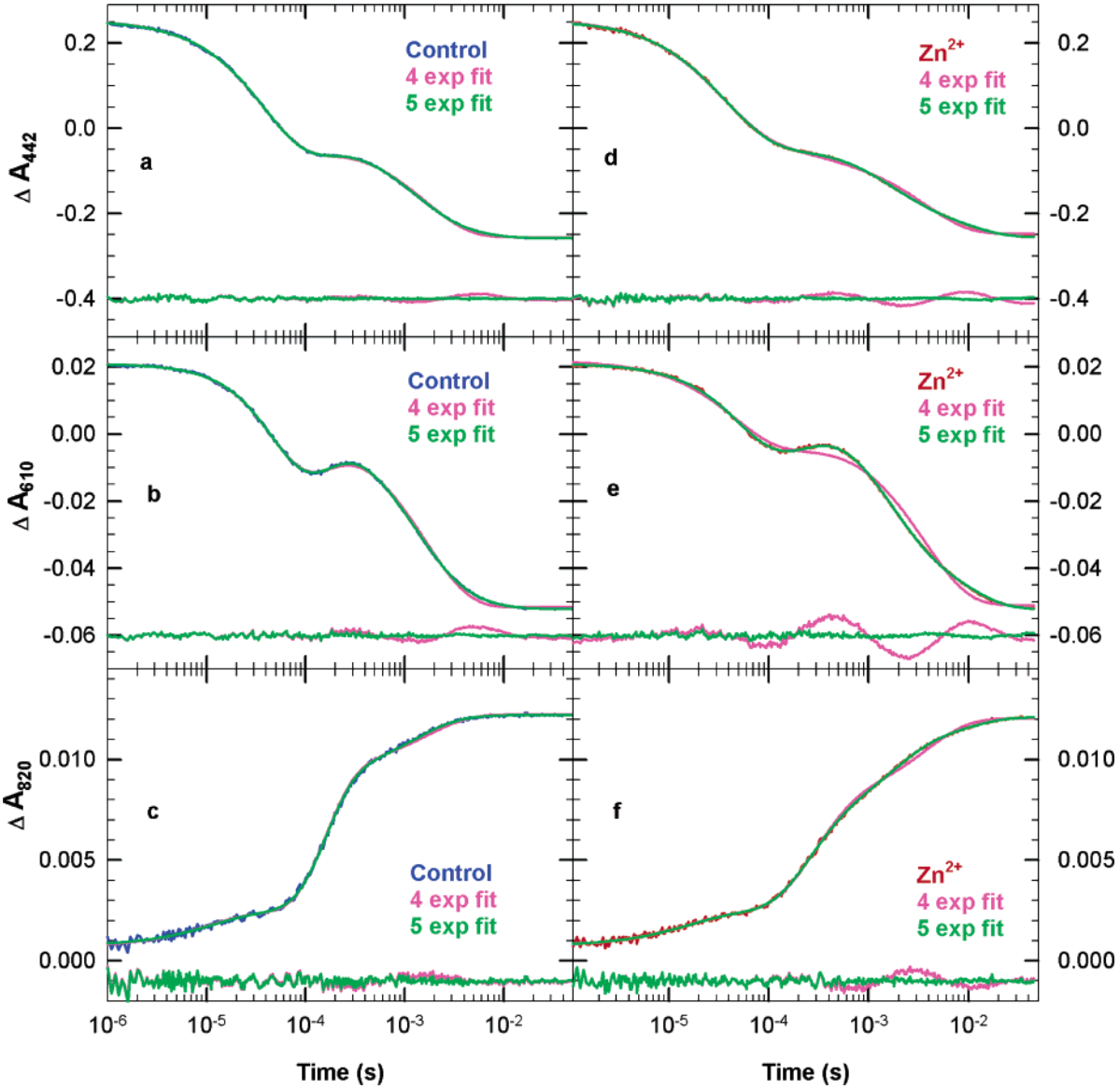

FIGURE 2: Transient absorbance changes in the absence of metal ions (a−c, blue) and in the presence of 300 μM Zn^{2+} (d−f, red) and the exponential fits to the data. The magenta and green curves represent four-exponential and five-exponential fits to the transient data, respectively. The residuals at the bottom of the panels represent the difference between the data and the four-exponential (magenta) and five-exponential (green) fits. They have been multiplied by a factor of 2 for clarity.

Table 1: Apparent Lifetimes

	control	Zn^{2+}	Cd^{2+}	Ni^{2+}		control	Zn^{2+}	Cd^{2+}	Ni^{2+}
τ_1 (μs)	23	22	22	20	τ_4 (ms)	1.2	1.5	1.7	2.2
τ_2 (μs)	38	45	43	40	τ_5 (ms)	3.9	8.4	7.6	8.6
τ_3 (μs)	90	190	190	210					

been reported previously for electron transfer in the bovine enzyme in the absence of metal ions (*62*), and biphasic kinetics were observed for the $\mathbf{F_s} \rightarrow \mathbf{O_s}$ transition in *R. sphaeroides* at 445 nm at >10 μM Zn^{2+} (*45*). The additional 1.5 μs lifetime observed in the Soret and visible regions in our multichannel studies (*16*, *52*) was not within the time resolution of the single-wavelength detection system.

Application of the Kinetic Analysis to the Experimental Data. The exponential fit to the transient data produces the apparent rates and the corresponding amplitudes, the latter of which are also called pre-exponential factors. To interpret the single-wavelength reaction kinetics, we must propose a mechanism. Scheme 1 shows the conventional unidirectional sequential scheme with five proposed intermediates, which allow us to test the sequential model quantitatively.

The reversibility of the binding of dioxygen to the reduced enzyme has been reported (*3*, *6*−*10*), but it is not included in Scheme 1 because the introduction of such a reversible step does not affect our formal description of the kinetics or the conclusion of our analysis. Using the approach outlined in Materials and Methods, we derive the amplitudes of the sequential intermediates from the absorbance changes associated with the different exponentials and the kinetic equations of the sequential scheme. A good agreement between the experimental amplitudes and the expected model amplitudes of the respective intermediates at the recorded wavelengths would provide support for the sequential mechanism. Inconsistency between those amplitudes would indicate that the sequential mechanism is inadequate for describing the kinetics of the reaction.

Figure 3 (left panel) shows the model spectra in the Soret region (435−455 nm) of heme a_3/Cu_B in different redox and

Scheme 1

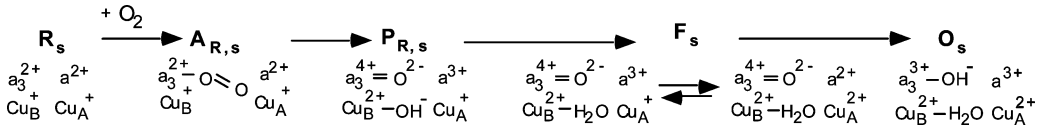

ligation states referenced against a_3^{2+}-CO Cu_B^+. The reduced-minus-oxidized spectrum of heme *a* ($a^{2+} - a^{3+}$) (curve f) and the oxidized spectrum of Cu_A^{2+} (curve g) (*60*) are shown for comparison. Figure 3 (right panel) shows the corresponding spectra in the visible region between 595 and 620 nm. These spectra, termed model amplitudes, contain all the information necessary to calculate the absorption amplitudes of all the above-mentioned intermediates presumed to be present in the reaction sequence. The recorded spectra of the oxidized, reduced, mixed-valence CO, and fully reduced CO enzyme, the oxidized Cu_A, **P**, and **F**, which form the basis for the model spectra, were not affected by the presence of metal ions. The absorbance amplitude of compound **A** in the mixed-valence enzyme is the same in the absence and presence of metal ions (see below).

Figure 4a−d shows the experimental transient data on a logarithmic time scale in the absence (a and c, solid lines) and presence of Zn^{2+} (b and d, solid lines) at 442 and 610 nm. Since five exponentials were required to adequately fit the data, we have to consider a kinetic scheme that accommodates six intermediates. The unidirectional sequential model of six intermediates is assumed to be similar to the conventional model (Scheme 1), containing all the intermediates listed in that model, in addition to an intermediate decaying with a longer millisecond lifetime, $\mathbf{(F/O)_s}$ (Scheme 2).

Scheme 2

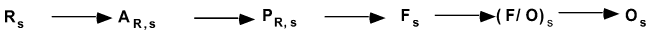

The circles in Figure 4a−d represent the experimental amplitudes of the six sequential intermediates. They are derived using the five experimental apparent rates and the pre-exponential factors (*b* vectors) according to eq 7. They are referenced versus the amplitude of the fully reduced CO-bound enzyme.

To test the conventional unidirectional sequential mechanism depicted in Scheme 1 and the six-intermediate sequential mechanism (Scheme 2), we compared the experimental absorbance traces (solid lines) and intermediate amplitudes (circles) to the ones expected based on the scheme. The squares in Figure 4a−d represent the model amplitudes of intermediates $\mathbf{R_s}$, $\mathbf{A_{R,s}}$, $\mathbf{P_{R,s}}$, $\mathbf{F_s}$, and $\mathbf{O_s}$, presumed to be present according to the conventional sequential scheme (Scheme 1). The model amplitude of $\mathbf{P_{R,s}}$ is that of $\mathbf{P_M}$, corrected for the different redox state of Cu_A. As mentioned above, these amplitudes are calculated directly from the spectral information shown in Figure 3 and are referenced versus a_3^{2+}-CO Cu_B^+. The $\mathbf{F_s}$ intermediate is assumed to be a 2:1 mixture of $\mathbf{F_{II}}$ and $\mathbf{F_I}$, which corresponds to a 2:1 ratio of reduced and oxidized heme *a* (*16*, *53*, *59*). The amplitudes are placed at the positions of the maximum concentrations of the intermediates on the time axis. The numerical values of the experimental and model amplitudes of the individual intermediates are listed in Table 2. Note that intermediates are defined as states and their amplitude is $c_o \times \epsilon$. Intermediate amplitudes therefore always represent the absorbance for 100% of each intermediate. It is clear that some of the experimental amplitudes (Figure 4, circles) of the six intermediates do not match the corresponding model amplitudes (Figure 4, squares) in the presence or absence of metal ions. This indicates that unidirectional schemes involving the intermediates depicted in Schemes 1

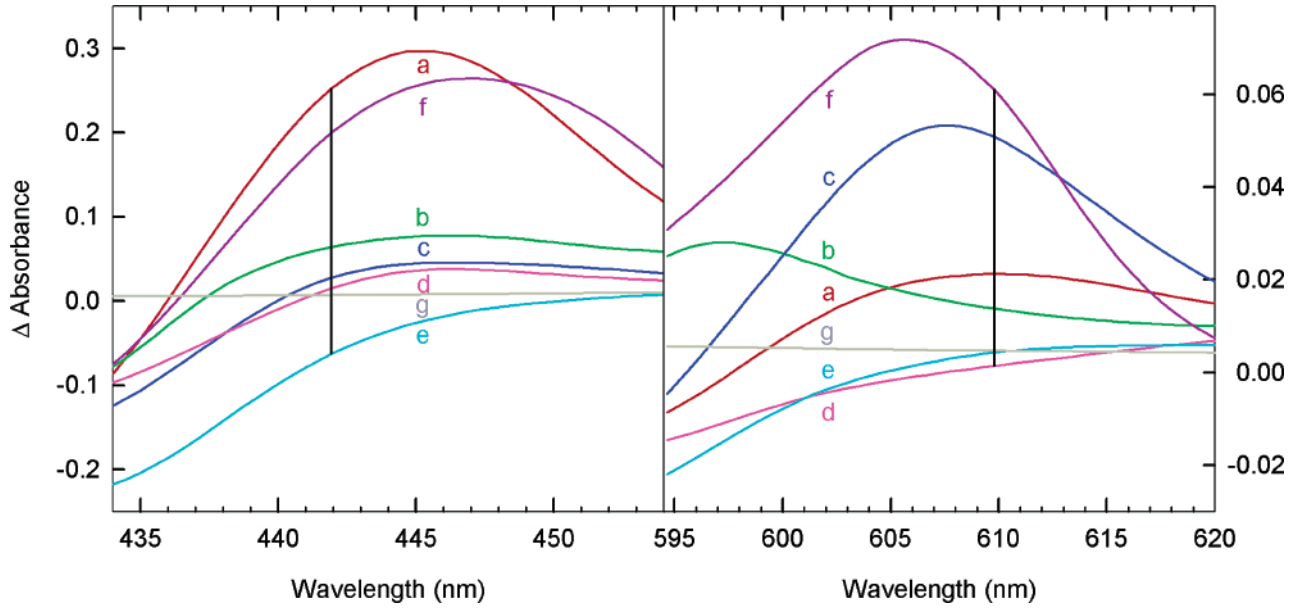

FIGURE 3: (a−e) Model spectra of heme a_3/Cu_B in different redox and ligation states referenced against a_3^{2+}CO Cu_B^+, in the Soret region (435−455 nm) and visible region (595−620 nm): (a) reduced heme a_3/Cu_B (a_3^{2+} Cu_B^+−a_3^{2+}CO Cu_B^+), (b) compound **A** (a_3^{2+}−O_2 Cu_B^+−a_3^{2+}CO Cu_B^+), (c) $\mathbf{P_R}$ ($\mathbf{P_M}$) (a_3^{4+}=O^{2-} Cu_B^{2+}−a_3^{2+}CO Cu_B^+), (d) **F** (a_3^{4+}=O^{2-} Cu_B^{2+}−a_3^{2+}CO Cu_B^+), and (e) oxidized heme a_3/Cu_B (a_3^{3+} Cu_B^{2+}−a_3^{2+}CO Cu_B^+). (f and g) Model spectra of heme *a* and Cu_A. (f) The reduced-minus-oxidized spectrum of heme *a* ($a^{2+} - a^{3+}$) and (g) the oxidized spectrum of Cu_A^{2+} (*60*). The monitoring wavelengths, 442 and 610 nm, are represented by black vertical lines.

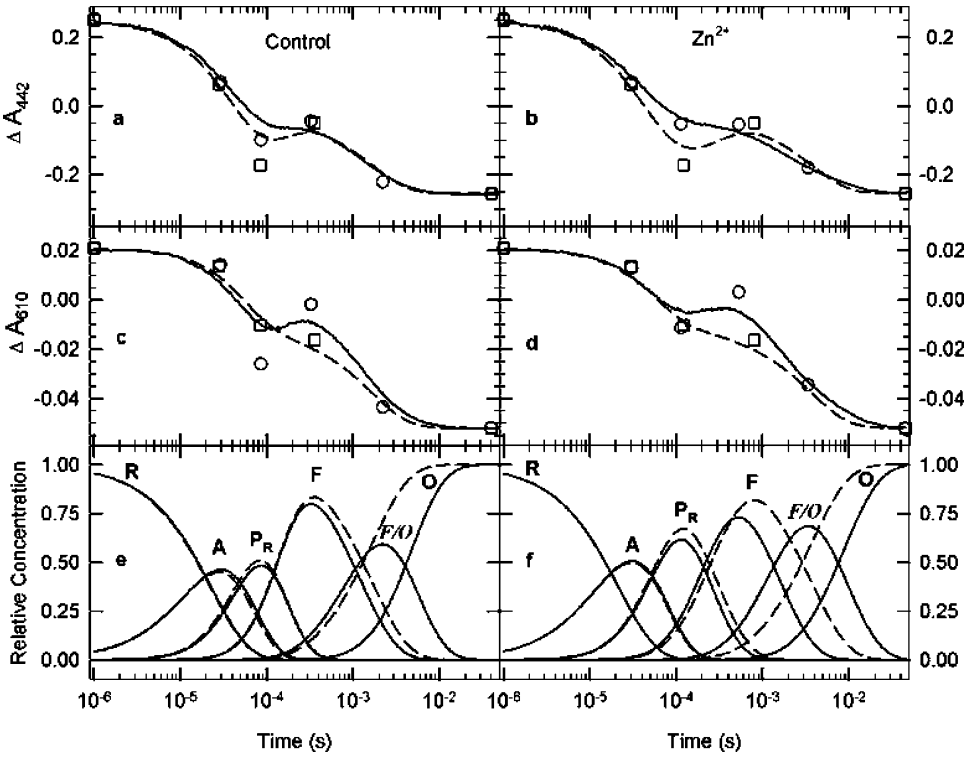

FIGURE 4: (a−d) Comparison of the experimental transient data and intermediate amplitudes with predictions by the conventional unidirectional sequential mechanism (Scheme 1) and a sequential scheme containing an additional millisecond intermediate (Scheme 2). Solid lines represent the transient data at 442 (a and b) and 610 nm (c and d) in the absence (a and c) and presence of Zn^{2+} (b and d). The dashed traces (a−d) represent theoretical absorbance changes expected on the basis of the conventional five-intermediate unidirectional sequential mechanism (Scheme 1) (see the text for details). The squares represent the absorbance amplitudes of the model spectra for the five individual intermediates. The circles represent the experimental amplitudes of the six intermediates derived based on a six-intermediate unidirectional sequential scheme (Scheme 2) using the five experimental apparent rates and the pre-exponential factors (*b* vectors) according to eq 7. The experimental and model amplitudes are referenced vs the amplitude of the reduced CO-bound enzyme. (e and f) Time-dependent concentration profiles of the intermediates for the unidirectional scheme using the apparent rate constants from the four-exponential (dashed lines) and five-exponential fits (solid lines) as microscopic rate constants. The monitoring wavelengths, 610 and 442 nm, are represented by black vertical lines.

Table 2: Amplitudes of Intermediates ($\times 10^3$ optical density units)

intermediate	model[a]	control	Zn^{2+}	Cd^{2+}	Ni^{2+}
442 nm					
$\mathbf{R}_s$	250	260	260	250	260
$\mathbf{A}_{R,s}$	64	71	70	72	72
$\mathbf{P}_{R,s}$	−170	−99	−52	−58	−66
$\mathbf{F}_s$	−48	−44	−54	−50	−70
$\mathbf{(F/O)}_s$		−220	−180	−180	−160
$\mathbf{O}_s$	−260	−260	−260	−250	−250
610 nm					
$\mathbf{R}_s$	21	21	21	21	21
$\mathbf{A}_{R,s}$	14	14	13	14	12
$\mathbf{P}_{R,s}$	−10	−26	−11	−14	−15
$\mathbf{F}_s$	−16	−2	−3	−1	−5
$\mathbf{(F/O)}_s$		−43	−34	−36	−29
$\mathbf{O}_s$	−52	−52	−52	−52	−52
820 nm					
$\mathbf{R}_s$		0.7	0.7	0.6	0.4
$\mathbf{A}_{R,s}$		4.0	3.0	3.5	3.4
$\mathbf{P}_{R,s}$		0.1	1.6	1.0	1.3
$\mathbf{F}_s$		9.4	7.0	7.2	5.9
$\mathbf{(F/O)}_s$		12.0	10.7	11.3	10.5
$\mathbf{O}_s$		12.2	12.1	12.2	12.0

[a] The model amplitudes refer to the **R**, **A**, $\mathbf{P_R}$, **F** ($\mathbf{F_I/F_{II}}$), and **O** forms. The model amplitude of $\mathbf{P_R}$ is that of $\mathbf{P_M}$, corrected for the redox state of Cu_A.

and 2 are inadequate to describe the reaction kinetics. This conclusion is based on the assumption of spectral equality between the model and transient states.

This conclusion is further supported by the broken traces in panels a−d, which represent the theoretical absorbance traces expected for the conventional unidirectional sequential mechanism depicted in Scheme 1. The theoretical absorbance trace was calculated according to eq 4 using the model amplitudes (Figure 4, squares) and the concentration of the intermediates (dashed curves in Figure 4e,f). The apparent disagreement between the calculated absorbance traces (Figure 4a−d, broken trace) based on the five-intermediate conventional unidirectional sequential scheme (Scheme 1) and the transient experimental data (Figure 4a−d, solid lines) implies that the five-intermediate conventional sequential mechanism may not be an adequate model for describing the reaction kinetics.

Panels e and f of Figure 4 show the time−concentration profiles for the intermediates of five-intermediate (dashed lines) and six-intermediate (solid lines) unidirectional sequential schemes in the absence (panel e) and presence of Zn^{2+} (panel f). The profiles are calculated from eq 2 using the apparent lifetimes of the four- and five-exponential fits to the experimental data, respectively. Note that the amplitudes of the concentration profiles represent the maximum populations of the corresponding intermediate states and they have no relationship to the absorbance amplitudes of the intermediates, $c_o \times \epsilon$, discussed above.

Reaction of the Mixed-Valence Enzyme with Dioxygen. To better assess the absorbance contribution associated with

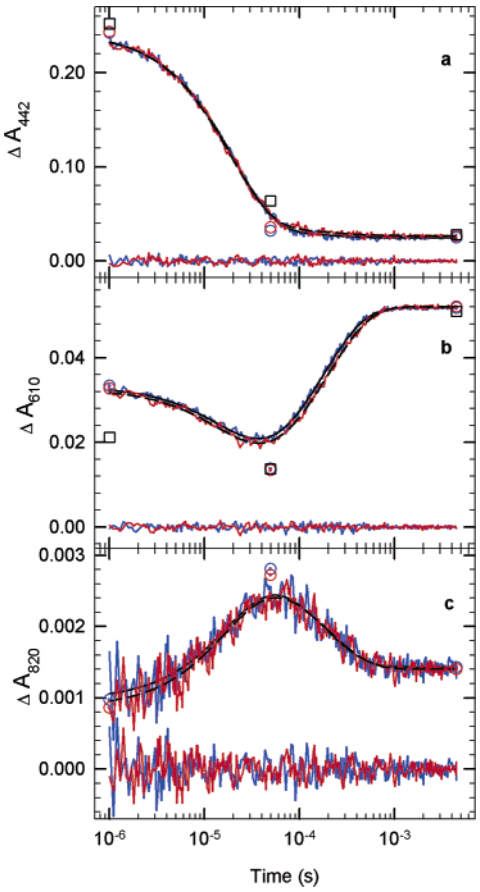

FIGURE 5: Transient absorbance changes taking place after photolysis of the mixed-valence CO-bound enzyme in the presence of dioxygen. The data are normalized and displaced on a logarithmic time scale. The conditions are the same as in Figure 1. The data were recorded in the absence of metal ions (blue curve) and in the presence of 300 μM Zn^{2+} (red curve). The solid and dashed black traces represent a two-exponential fit to the data in the absence and presence of Zn^{2+}, respectively. The residuals at the bottom of the panels represent the difference between the data and the two-exponential fits in the presence (red) and absence of metal ions (blue). They have been multiplied by a factor of 2 for clarity. The circles represent the experimental amplitudes of intermediates $\mathbf{R_M}$, $\mathbf{A_M}$, and $\mathbf{P_M}$ in the absence (blue) and presence of Zn^{2+} (red) at their maximum concentration. The amplitudes are referenced vs the amplitude of the mixed-valence CO-bound enzyme. The experimental amplitude of $\mathbf{R_M}$ reflects ~27% back-electron transfer from heme a_3 to heme *a*. The squares represent the amplitudes of the corresponding model spectra. The model spectrum of $\mathbf{R_M}$ is not corrected for back-electron transfer.

heme a_3 upon conversion of compound **A** to **P**, without the interference from the oxidation of heme *a*, we monitored the absorbance changes associated with the reaction of dioxygen with the mixed-valence enzyme in the absence and presence of Zn^{2+}. Figure 5 shows transient data at 442, 610, and 820 nm in the absence (blue) and presence (red) of Zn^{2+}. It is clear that Zn^{2+} does not have a detectable effect on the reaction of dioxygen with the mixed-valence enzyme. Both data sets were adequately fitted with two exponentials (solid line, no Zn^{2+}; broken line, with Zn^{2+}) as reflected in the random-noise residuals (Figure 5). Practically the same apparent lifetimes were observed in the absence (20 ± 3 and 180 ± 20 μs) and presence of Zn^{2+} (19 ± 3 and 200 ± 20 μs). The data were interpreted as a two-step, unidirectional sequential model: $\mathbf{R_M}$ (a_3^{2+} Cu_B^{+} a^{3+} Cu_A^{2+}) → $\mathbf{A_M}$ (a_3^{2+}−O_2 Cu_B^{+} a^{3+} Cu_A^{2+}) → $\mathbf{P_M}$ (a_3^{4+}=O^{2-} Cu_B^{2+}−OH^- Tyr· a^{3+} Cu_A^{2+}). Figure 5 also shows the experimental amplitudes of individual intermediates $\mathbf{R_M}$, $\mathbf{A_M}$, and $\mathbf{P_M}$ in the presence (red circles) and absence (blue circles) of Zn^{2+}. The amplitudes are referenced versus the amplitude of the mixed-valence CO-bound enzyme. The experimental amplitude of $\mathbf{R_M}$ contains the contribution from the back-electron transfer from heme a_3 to heme *a* on an early microsecond time scale (*63*−*67*). The back-flow was estimated to be ~27%. The model amplitudes (squares) at 442 and 610 nm were generated without correcting for back-electron transfer, which explains the discrepancies between the experimental and model amplitudes of $\mathbf{R_M}$. The good agreement between the experimental intermediate amplitudes of $\mathbf{A_M}$ and $\mathbf{P_M}$, calculated on the basis of a two-step sequential scheme, and the respective model amplitudes indicates that the reaction of the mixed-valence enzyme with dioxygen is well represented by the $\mathbf{R_M} \rightarrow \mathbf{A_M} \rightarrow \mathbf{P_M}$ unidirectional sequential scheme.

DISCUSSION

The interpretation of the single-wavelength data in terms of intermediate amplitudes can be a powerful tool for designing and testing kinetic models. The quantitative description presented here for the classical unidirectional sequential model is simple and easy to use. It shows that all of the kinetic and spectral parameters involved in unidirectional sequential models can be obtained from the results of exponential fits. Our approach represents an alternative to a previous method in which the transient optical absorption results were analyzed by simulating the absorbance traces (*9*). The previous method involves the integration of linear differential equations to obtain the time courses of the concentrations of the proposed intermediates, followed by the calculation of the absorbance time course using estimated extinction coefficients (*9*). Both the microscopic rate constants and the extinction coefficients are obtained by an iterative process. The approach presented here allows a direct calculation of the absorbance amplitudes of the intermediates in the unidirectional sequential scheme using the pre-exponential factors associated with the different exponentials in the multiexponential fit and the kinetic equations of the respective scheme. Solving first-order kinetic equations analytically or by numerical integration and fitting them to experimental data can thus be avoided. Our approach can also be extended to more complex schemes.

The kinetic description makes it easy to understand why the *b* values cannot be equated with the true absorbance difference between two intermediates. In general, the amplitude of the exponential fit (*b* value) corresponding to a particular apparent rate appears to be a linear combination of the absorbances of those intermediates in the sequential scheme that do not decay faster than the respective apparent rate. For example, according to eq 6, b_1 can be represented by the following equation:

$$b_1 = c_o \times [\epsilon_K \ \epsilon_L \ \epsilon_M \ \epsilon_N] \times \begin{bmatrix} 1 \\ -k_1/(k_1 - k_2) \\ k_1k_2/(k_1 - k_2)(k_1 - k_3) \\ -k_2k_3/(k_1 - k_2)(k_1 - k_3) \end{bmatrix}$$

Table 3: Comparison of the Amplitudes of the Five-Exponential Fit ($\times 10^3$ optical density units) and the True Absorbance Differences between the Individual Intermediates Represented in Scheme 2

	442 nm	610 nm	820 nm
	Control		
b_1	−100	−68	−14
$\mathbf{R_s}$-$\mathbf{A_{R,s}}$	189	7	−3.3
b_2	540	150	28
$\mathbf{A_{R,s}}$-$\mathbf{P_{R,s}}$	170	40	3.9
b_3	−160	−65	−22
$\mathbf{P_{R,s}}$-$\mathbf{F_s}$	−55	−24	−9.3
b_4	180	43	−2.9
$\mathbf{F_s}$-$\mathbf{(F/O)_s}$	176	41	−2.6
b_5	54	13	−0.3
$\mathbf{(F/O)_s}$-$\mathbf{O_s}$	40	9	−0.2
b_0	−260	−52	12.2
$\mathbf{O_s}$-RCO	−260	−52	12.2
	Zn^{2+}		
b_1	72	−16	−4.1
$\mathbf{R_s}$-$\mathbf{A_{R,s}}$	190	8	−2.3
b_2	240	56	5.7
$\mathbf{A_{R,s}}$-$\mathbf{P_{R,s}}$	122	24	1.4
b_3	−25	−30	−7.1
$\mathbf{P_{R,s}}$-$\mathbf{F_s}$	2	−8	−5.4
b_4	130	41	−4.2
$\mathbf{F_s}$-$\mathbf{(F/O)_s}$	126	31	−3.7
b_5	95	22	−1.7
$\mathbf{(F/O)_s}$-$\mathbf{O_s}$	80	18	−1.4
b_0	−260	−52	12.1
$\mathbf{O_s}$-RCO	−260	−52	12.1

while the absorbance difference between the first two intermediates is

$$\mathbf{A}_O - \mathbf{A}_P = c_o \times [\epsilon_K \ \epsilon_L \ \epsilon_M \ \epsilon_N] \times \begin{bmatrix} 1 \\ -1 \\ 0 \\ 0 \end{bmatrix}$$

The *b* value can only approach the absorbance difference between two intermediates when the rates are well separated. This is supported by Table 3, which shows a comparison of the numerical values of the absorbance changes associated with each of the five apparent rates (*b* values) and the true absorbance difference between individual intermediates at the three wavelengths. The latter were determined on the basis of a unidirectional sequential scheme (Scheme 2) as discussed above.

Qualitative and Quantitative Interpretation of the Different Steps in the Sequential Scheme. Several of our experimental observations discussed below suggest that the oxidation of cytochrome oxidase by dioxygen is more complex than what can be described by the five-intermediate conventional unidirectional sequential mechanism (Scheme 1) or a six-intermediate sequential scheme (Scheme 2).

A*$_{R,s}$*-to-P*$_{R,s}$ *Transition. The absorbance change in the Soret region associated with heme a_3 is very small upon conversion of $\mathbf{A_M}$ to $\mathbf{P_M}$ in the mixed-valence enzyme (Figure 5a). Thus, the absorbance decrease at 442 nm associated with the transition from $\mathbf{A_{R,s}}$ to $\mathbf{P_{R,s}}$ in the reduced enzyme (Figure 4a,b) is practically entirely due to the oxidation of heme *a*, in agreement with previous reports (*7*, *9*, *13*, *14*, *68*). However, the experimental amplitude associated with the $\mathbf{A_{R,s}}$-to-$\mathbf{P_{R,s}}$ step in the fully reduced enzyme in the absence of metal ions is 0.170, while an amplitude of 0.236 would be expected if all the heme *a* became oxidized (Table 2). Therefore, it appears that only 70% of heme *a* becomes oxidized during the conversion of $\mathbf{A_{R,s}}$ to $\mathbf{P_{R,s}}$. The difference between the experimental amplitudes of the intermediates and the model amplitudes is even greater in the presence of the metal ions (Table 2), and we estimate that only ∼50% of heme *a* becomes oxidized during the $\mathbf{A_{R,s}}$-to-$\mathbf{P_{R,s}}$ transition. This implies that $\mathbf{P_{R,s}}$ is not identical to the $\mathbf{P_M}$ form in which heme *a* is fully oxidized.

The incomplete oxidation of heme *a* in the time window corresponding to the $\mathbf{A_{R,s}}$-to-$\mathbf{P_{R,s}}$ transition has been reported previously (*3*, *7*, *9*, *10*, *16*, *22*, *68*−*70*). It has been explained in terms of branched schemes, with heme *a* and Cu_B serving as electron donors to the binuclear site in the two branches (*3*, *7*, *10*, *68*, *69*). Alternatively, the "apparent" incomplete oxidation of heme *a* on a microsecond time scale has been explained in terms of a sequential scheme with fast electron transfer from heme *a* to $\mathbf{A_{R,s}}$ followed by a rapid intramolecular electron exchange of heme *a* with Cu_A that partially re-reduces heme *a* (*9*). This explanation is based on the composition of the accumulated products in the time window of the $\mathbf{A_{R,s}}$-to-$\mathbf{P_{R,s}}$ transition and not on the incomplete oxidation of heme *a* in the $\mathbf{P_{R,s}}$ intermediate. Our results indicate that heme *a* is incompletely oxidized in intermediate $\mathbf{P_{R,s}}$ based on the discrepancy between the experimental intermediate amplitude and the respective model amplitude. As discussed below, our data suggest that heme *a* oxidation may occur on 40 μs and 100−200 μs time scales from compound **A** in addition to the millisecond oxidation, and multiwavelength studies from our laboratory support this conclusion (*53*).

P*$_{R,s}$*-to-F*$_s$ *Transition. A significant absorbance increase at 820 nm is associated with Cu_A oxidation on a 100−200 μs time scale in both the presence and absence of Zn^{2+} (Figure 2c,f and Table 2), the time scale of the sequential $\mathbf{P_{R,s}}$-to-$\mathbf{F_s}$ transition (*9*, *71*). Since Cu_A donates electrons to heme *a*, it follows that heme *a* re-reduction would occur concurrently with the Cu_A oxidation on this time scale. As heme a_3 does not contribute significantly to the absorbance changes at 442 nm upon the $\mathbf{P_{R,s}}$-to-$\mathbf{F_s}$ transition (Figure 5a and Figure 3, left panel), one would expect the heme *a* re-reduction on this time scale to be accompanied by a large absorbance increase at 442 nm. However, this is not observed; the transient traces in both the presence and absence of Zn^{2+} are practically flat at 442 nm on this time scale (Figure 4a,b, solid lines). This indicates that the absorbance increase at 442 nm due to re-reduction of heme *a* is compensated by an equivalent absorbance decrease due to heme *a* oxidation, thus reaching a quasi-steady state. The sequential model does not predict any heme *a* oxidation during the $\mathbf{P_{R,s}}$-to-$\mathbf{F_s}$ transition.

The Soret region amplitudes shown in Figure 4 (a and b) and Table 2 support these conclusions. The expected change for the $\mathbf{P_{R,s}} \rightarrow \mathbf{F_s}$ transition is 0.124 OD units, assuming that heme *a* is fully oxidized in $\mathbf{P_{R,s}}$. The control (no Zn^{2+} present) shows a change of only 0.055 OD units due to the incomplete oxidation of heme *a* in $\mathbf{P_{R,s}}$. In the presence of Zn^{2+} and the other metal ions, the experimental intermediate amplitudes remain practically unchanged during the $\mathbf{P_{R,s}} \rightarrow \mathbf{F_s}$ transition, indicating the same level of heme *a* oxidation exists in the two intermediates.

The absorbance change at 610 nm on the other hand does not indicate a quasi-steady-state absorbance on a 100−200 μs time scale but rather displays an increase in absorbance

(Figure 4c,d). If heme *a* is in a quasi-steady state, as suggested by the absence of absorbance changes at 442 nm, then the absorbance increase at 610 nm on the 100 μs time scale (200 μs in the presence of metal ions) must be associated with the formation of $\mathbf{P_R}$. Note that a large absorbance increase is observed at 610 nm in the mixed-valence enzyme upon formation of $\mathbf{P_M}$ (Figure 5b). Thus, it appears that the formation of $\mathbf{P_R}$ in the fully reduced enzyme is not completed on the 40 μs time scale but $\mathbf{P_R}$ continues to be formed on the same time scale (100−200 μs) as the quasi-steady state of heme *a* is reached. In the absence of Zn^{2+}, we have observed an equilibrium constant for the electron transfer between heme *a* and Cu_A at neutral pH in the 1.4−2.0 range (*16*, *53*, *59*). In the absence of metal ions, the 820 nm transient trace, which is primarily indicative of Cu_A oxidation, supports this ratio. In the presence of Zn^{2+}, the ratio is close to 1, consistent with impaired electron transfer from Cu_A to heme *a* (*46*).

The intermediate amplitudes from the 610 nm absorbance traces reveal further details about the $\mathbf{P_{R,s}} \rightarrow \mathbf{F_s}$ transition. At 610 nm, the absorbance contribution of **F** is negligible compared to those of heme *a*, $\mathbf{P_R}$, and **A** (Figure 3). The lower amplitude of $\mathbf{P_{R,s}}$ in the absence of Zn^{2+} (Table 2, control) compared to that of the model suggests that a fraction of $\mathbf{P_R}$ in the $\mathbf{P_{R,s}}$ intermediate is probably replaced by **F** and **A**. This is in agreement with our earlier proposal, which was based on discrepancies between the spectral shape of the $\mathbf{P_{R,s}}$ and the model spectrum of $\mathbf{P_R}$ ($\mathbf{P_M}$) (*52*, *53*). Recent resonance Raman studies also suggest that the $\mathbf{F_s}$ intermediate is formed on a time scale similar to that of the early oxidation of heme *a* (*10*). In the presence of metal ions, the experimental amplitude of $\mathbf{P_{R,s}}$ appears to match that of the model $\mathbf{P_R}$ (Table 2). However, this is a pure coincidence resulting from two opposing trends, less heme *a* oxidation (see Figure 3b) and replacement of $\mathbf{P_R}$ by less absorbing forms (**A** and **F**). The experimental amplitude of $\mathbf{F_s}$ ($\mathbf{F_I}$/$\mathbf{F_{II}}$) at 610 nm (Table 2) is clearly higher than that of the corresponding model spectrum, which contains a 2:1 ratio of reduced to oxidized heme *a*. The 820 nm signal precludes a higher ratio (i.e., more heme *a* being reduced), and therefore, we conclude that $\mathbf{P_R}$ is present in the $\mathbf{F_s}$ intermediate.

F_s-to-O_s Transition. Our studies indicate that two lifetimes, 1−2 and 4−9 ms, are required to adequately fit the data on the millisecond time scale in both the presence and absence of metal ions (Table 1). The 4−9 ms lifetime was not clearly resolved in our previous flow-flash multichannel experiments on the fully reduced enzyme (*16*, *52*, *53*, *70*), but the high accuracy of the time-dependent traces in the single-wavelength experiments allows this lifetime to be clearly observed. A re-reduction of the enzyme also frequently occurs at the completion of the flow-flash experiment between 10 and 50 ms, particularly if the concentration of the mediator is high, and this can obscure processes involving cytochrome oxidase oxidation on this time scale. In the experiments reported here, the concentration of the ruthenium hexammine mediator was 0.125 μM and there was no evidence for re-reduction on a millisecond time scale. While the residuals of the four-exponential fit in the absence of metal ions are small and require high accuracy of detection, the need for an additional lifetime in the presence of metal ions is obvious (Figure 2). The similarity between the different metal ions indicates a general kinetic effect rather than an isolated phenomenon specific to a single metal ion.

Scheme 3

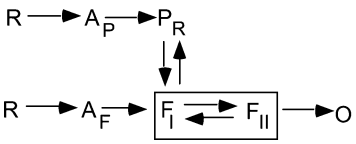

Scheme 4

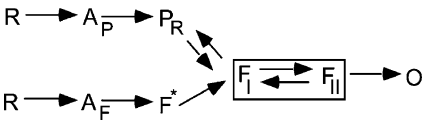

A millisecond lifetime of ∼5 ms, associated with electron transfer during the reaction of the fully reduced enzyme with dioxygen in the absence (*62*) and presence of metal ions (*45*), has been reported. Proton uptake through the K-pathway (*37*, *38*, *62*) and an electrogenic process (*72*, *73*) with a similar lifetime have also been observed. Wikström and co-workers have suggested that the $\mathbf{F_s}$ intermediate is converted to a high-energy oxidized state of the enzyme, **O**∼, which subsequently relaxes to the oxidized state, $\mathbf{O_s}$, thus accounting for the two millisecond lifetimes (*74*). The "5 ms phase" was proposed to be associated with protonation of the hydroxide on heme a_3 (*74*−*76*). Brzezinski and co-workers recently suggested that the **O**∼ state has two hydroxide molecules bound at the binuclear center while $\mathbf{O_s}$ may have only one OH^- bound to Cu_B (*77*). We observe absorbance changes associated with the longer millisecond time scale at all three wavelengths, and Brzezinski and co-workers also reported identical kinetic difference spectra for the two millisecond phases (*62*). Therefore, it seems unlikely that this process is due solely to heme a_3. Instead the absorbance decrease at 442 and 610 nm on this time scale probably results from the oxidation of heme *a*, and the corresponding increase at 820 nm, which is clearly observed in the presence of metal ions, can be attributed to oxidation of Cu_A.

The results described here have led us to consider a more complex reaction mechanism for cytochrome oxidase oxidation by dioxygen than the conventional unidirectional sequential mechanism. The data in the presence and absence of metal ions are consistent with $\mathbf{P_{R,s}}$ not being a single species but rather a mixture of species. This was encountered previously in our multichannel studies on the reaction of the reduced enzyme with dioxygen in the absence of metal ions (*52*, *53*). These studies indicated that a pH-dependent mixture of compound **A**, $\mathbf{P_R}$, and **F** is formed on the time scale of the sequential $\mathbf{P_{R,s}}$ intermediate. We interpreted the results in terms of a branched scheme, in which one branch generates the 607 nm $\mathbf{P_R}$ form and the other branch the **F** form, with a pH-dependent rate of exchange between the two branches (*53*) (Scheme 3). (In our previous paper, we used the notation "**P**" to represent the single chemical structure $\mathbf{P_R}$, which is spectrally equivalent to $\mathbf{P_M}$.) In these multichannel experiments, the second millisecond lifetime was not observed. To accommodate the second millisecond rate observed here, the model needs to be modified. A potential mechanism that satisfies this requirement is presented in Scheme 4.

Both schemes contain two parallel pathways with two isospectral species, $\mathbf{A_P}$ and $\mathbf{A_F}$, having different kinetic

Scheme 5

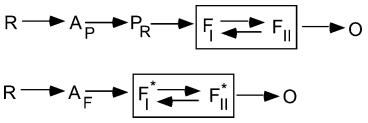

properties. To account for the $\mathbf{P_{R,s}}$ intermediate in the sequential scheme being a mixture of **A**, $\mathbf{P_R}$, and **F** forms, the decay rates of $\mathbf{A_P}$ and $\mathbf{A_F}$ in the two branches are different. The equilibrium between $\mathbf{P_R}$ and $\mathbf{F_I/F_{II}}$ accounts for the observation of $\mathbf{P_R}$ being present in intermediate $\mathbf{F_I/F_{II}}$. The longer millisecond lifetime corresponds to the conversion of **F*** to the equilibrium mixture of $\mathbf{F_I/F_{II}}$.

Alternatively, the data can be represented by Scheme 5, which consists of two independent pathways. Both Schemes 4 and 5 require two **F** species to account for the observed lifetimes. The possibility of two **F** species being present was also raised when we proposed the branched mechanism in Scheme 3 (*53*). Schemes 4 and 5 are reminiscent of schemes proposed for the reaction of hydrogen peroxide with the oxidized enzyme, which incorporate two ferryl species with slightly different spectral properties (*78*−*80*). On the basis of the single-wavelength experiments presented here, we cannot determine whether **F** and **F*** are spectrally different. The branched schemes proposed here produce many more lifetimes than can be determined experimentally (*53*). This quasi-degeneracy cannot be adequately treated on the basis of a few amplitude values obtained in single-wavelength experiments. Multiwavelength studies with both spectral and temporal information are required for analysis of such complex schemes.

CONCLUSIONS

The kinetic approach introduced here shows that lifetimes and amplitudes can be transformed into physically meaningful intermediate properties, namely, intermediate absorbances. Although we have applied this approach to the most frequently used unidirectional sequential scheme, the same approach is applicable to other proposed kinetic models that can be described by first-order linear differential equations.

The kinetic analysis of the transient single-wavelength data suggests that the oxidation of heme *a*, proposed to accompany the formation of the $\mathbf{P_{R,s}}$ intermediate in the sequential scheme, is far from complete. A significant fraction of heme *a*, 30−50%, is still reduced in the $\mathbf{P_{R,s}}$ intermediate when the transient data are analyzed using a sequential mechanism. Moreover, $\mathbf{P_R}$ is partially formed in the 40 μs time window, and its formation is completed on the 100 μs time scale (200 μs in the presence of metal ions), during which $\mathbf{F_s}$ is formed in the conventional sequential scheme. This suggests that the $\mathbf{A_P} \rightarrow \mathbf{P_R}$ transition in the $\mathbf{P_R}$ branch (Schemes 4 and 5) is slower than the $\mathbf{A_F} \rightarrow \mathbf{F}$ transition in the **F** branch. The transfer of the fourth electron from the equilibrated heme *a*/Cu_A site to the heme a_3 center occurs on two time scales rather than in the single step proposed by the conventional sequential scheme (Scheme 1). This is the case both in the presence and in the absence of metal ions.

Our observations are consistent with previous results of Brzezinski and co-workers, who reported a 2-fold decrease in the rate of the $\mathbf{P_{R,s}}$-to-$\mathbf{F_s}$ transition in the presence of Zn^{2+} (*45*, *46*). These authors also reported a decrease in the rate of the $\mathbf{F_s}$-to-$\mathbf{O_s}$ transition of a factor of 2−3 in the presence of metal ions. However, our studies indicate that the metal ions affect primarily the rate and amplitude of the longer millisecond process and to a smaller extent the early 1−2 ms process.

Our studies and others (*9*, *12*, *37*, *69*) show that the high quality of time-dependent traces in single-wavelength measurements can accurately establish the number of exponential processes present and their apparent rates. When combined with amplitude analysis, the kinetic approach presented here can be used to test the validity of certain kinetic schemes. However, a detailed picture of the reaction kinetics cannot be obtained from single-wavelength data but rather requires spectral information from multiwavelength kinetic studies.

REFERENCES

1. Wikström, M. K. F. (1977) Proton pump coupled to cytochrome *c* oxidase in mitochondria, *Nature 266*, 271−273.
2. Babcock, G. T., and Wikström, M. (1992) Oxygen activation and the conservation of energy in cell respiration, *Nature 356*, 301−309.
3. Ferguson-Miller, S., and Babcock, G. T. (1996) Heme/copper terminal oxidases, *Chem. Rev. 96*, 2889−2907.
4. Zaslavsky, D., and Gennis, R. B. (2000) Proton pumping by cytochrome oxidase: progress, problems and postulates, *Biochim. Biophys. Acta 1458*, 164−179.
5. Gennis, R. B. (1998) Multiple proton-conducting pathways in cytochrome oxidase and a proposed role for the active-site tyrosine, *Biochim. Biophys. Acta 1365*, 241−248.
6. Orii, Y. (1984) Formation and decay of the primary oxygen compound of cytochrome oxidase at room temperature as observed by stopped-flow, laser flash photolysis and rapid scanning, *J. Biol. Chem. 259*, 7187−7190.
7. Hill, B. C., and Greenwood, C. (1984) The reaction of fully reduced cytochrome *c* oxidase with oxygen studied by flow-flash spectrophotometry at room temperature, *Biochem. J. 218*, 913−921.
8. Varotsis, C., Zhang, Y., Appelman, E. H., and Babcock, G. T. (1993) Resolution of the reaction sequence during the reduction of O_2 by cytochrome oxidase, *Proc. Natl. Acad. Sci. U.S.A. 90*, 237−241.
9. Hill, B. C. (1994) Modeling the sequence of electron-transfer reactions in the single turnover of reduced, mammalian cytochrome *c* oxidase with oxygen, *J. Biol. Chem. 269*, 2419−2425.
10. Han, S., Takahashi, S., and Rousseau, D. L. (2000) Time dependence of the catalytic intermediates in cytochrome *c* oxidase, *J. Biol. Chem. 275*, 1910−1919.
11. Orii, Y. (1988) Intermediates in the reaction of reduced cytochrome oxidase with dioxygen, *Ann. N.Y. Acad. Sci. 550*, 105−117.
12. Oliveberg, M., Brzezinski, P., and Malmström, B. G. (1989) The effect of pH and temperature on the reaction of fully reduced and mixed-valence cytochrome *c* oxidase with dioxygen, *Biochim. Biophys. Acta 977*, 322−328.
13. Verkhovsky, M. I., Morgan, J. E., and Wikström, M. (1994) Oxygen binding and activation: Early steps in the reaction of oxygen with cytochrome *c* oxidase, *Biochemistry 33*, 3079−3086.
14. Morgan, J. E., Verkhovsky, M. I., and Wikström, M. (1996) Observation and assignment of peroxy and ferryl intermediates in the reduction of dioxygen to water by cytochrome *c* oxidase, *Biochemistry 35*, 12235−12240.
15. Karpefors, M., Ädelroth, P., Aagaard, A., Sigurdson, H., Svensson-Ek, M., and Brzezinski, P. (1998) Electron−proton interactions in terminal oxidases, *Biochim. Biophys. Acta 1365*, 159−169.
16. Sucheta, A., Szundi, I., and Einarsdóttir, Ó. (1998) Intermediates in the reaction of fully reduced cytochrome *c* oxidase with dioxygen, *Biochemistry 37*, 17905−17914.
17. Varotsis, C., Woodruff, W. H., and Babcock, G. T. (1990) Direct detection of a dioxygen adduct of cytochrome a_3 in the mixed-valence cytochrome oxidase/dioxygen reaction, *J. Biol. Chem. 265*, 11131−11136.
18. Ogura, T., Takahashi, S., Shinzawa-Itoh, K., Yoshikawa, S., and Kitagawa, T. (1990) Observation of the Fe^{II}-O_2 stretching Raman

band for cytochrome oxidase compound A at ambient temperature, *J. Am. Chem. Soc. 112*, 5630−5631.
19. Han, S., Ching, Y.-C., and Rousseau, D. L. (1990) Ferryl and hydroxy intermediates in the reaction of oxygen with reduced cytochrome *c* oxidase, *Nature 348*, 89−90.
20. Proshlyakov, D. A., Pressler, M. A., and Babcock, G. T. (1998) Dioxygen activation and bond cleavage by mixed-valence cytochrome *c* oxidase, *Proc. Natl. Acad. Sci. U.S.A. 95*, 8020−8025.
21. Chance, B., Saronio, C., and Leigh, J. S., Jr. (1975) Functional intermediates in the reaction of membrane-bound cytochrome oxidase with oxygen, *J. Biol. Chem. 250*, 9226−9237.
22. Clore, M. G., Andréasson, L.-E., Karlsson, B. G., Aasa, R., and Malmström, B. (1980) Characterization of the low-temperature intermediates of the reaction of fully reduced soluble cytochrome oxidase with oxygen by electron-paramagnetic-resonance and optical spectroscopy, *Biochem. J. 185*, 139−154.
23. Hansson, Ö., Karlsson, B., Aasa, R., Vänngård, T., and Malmström, B. G. (1982) The structure of the paramagnetic oxygen intermediate in the cytochrome *c* oxidase reaction, *EMBO J. 1*, 1295−1297.
24. Blair, D. F., Witt, S. N., and Chan, S. I. (1985) Mechanism of cytochrome *c* oxidase-catalyzed dioxygen reduction at low temperatures. Evidence for two intermediates at the three-electron level and entropic promotion of the bond-breaking step, *J. Am. Chem. Soc. 107*, 7389−7399.
25. Witt, S. N., and Chan, S. I. (1987) Evidence for a ferryl Fe_{a3} in oxygenated cytochrome *c* oxidase, *J. Biol. Chem. 262*, 1446−1448.
26. Nilsson, T., Hallén, S., and Oliveberg, M. (1990) Rapid proton release during flash-induced oxidation of cytochrome *c* oxidase, *FEBS Lett. 260*, 45−47.
27. Oliveberg, M., Hallén, S., and Nilsson, T. (1991) Uptake and release of protons during the reaction between cytochrome *c* oxidase and molecular oxygen: A flow-flash investigation, *Biochemistry 30*, 436−440.
28. Hallén, S., and Nilsson, T. (1992) Proton transfer during the reaction between fully reduced cytochrome *c* oxidase and dioxygen: pH and deuterium isotope effects, *Biochemistry 31*, 11853−11859.
29. Paula, S., Sucheta, A., Szundi, I., and Einarsdóttir, Ó. (1999) Proton and electron transfer during the reduction of molecular oxygen by fully reduced cytochrome *c* oxidase: A flow-flash investigation using optical multichannel detection, *Biochemistry 38*, 3025−3033.
30. Mitchell, R., Mitchell, P., and Rich, P. R. (1992) Protonation states of the catalytic intermediates of cytochrome *c* oxidase, *Biochim. Biophys. Acta 1101*, 188−191.
31. Capitanio, N., Vygodina, T. V., Capitanio, G., Konstantinov, A. A., Nicholls, P., and Papa, S. (1997) Redox-linked protolytic reactions in soluble cytochrome-*c* oxidase from beef-heart mitochondria: redox Bohr effects, *Biochim. Biophys. Acta 1318*, 255−265.
32. Tsukihara, T., Aoyama, H., Yamashita, E., Tomizaki, T., Yamaguchi, H., Shinzawa-Itoh, K., Nakashima, R., Yaono, R., and Yoshikawa, S. (1996) The whole structure of the 13-subunit oxidized cytochrome *c* oxidase at 2.8 Å, *Science 272*, 1136−1144.
33. Iwata, S., Ostermeier, C., Ludwig, B., and Michel, H. (1995) Structure at 2.8 Å resolution of cytochrome *c* oxidase from *Paracoccus denitrificans*, *Nature 376*, 660−669.
34. Ostermeier, C., Harrenga, A., Ermler, U., and Michel, H. (1997) Structure at 2.7 Å resolution of the *Paracoccus denitrificans* two-subunit cytochrome *c* oxidase complexed with an antibody FV fragment, *Proc. Natl. Acad. Sci. U.S.A. 94*, 10547−10553.
35. Konstantinov, A. A., Siletsky, S., Mitchell, D., Kaulen, A., and Gennis, R. B. (1997) The roles of the two proton input channels in cytochrome *c* oxidase from *Rhodobacter sphaeroides* probed by the effects of site-directed mutations on time-resolved electrogenic intraprotein proton transfer, *Proc. Natl. Acad. Sci. U.S.A. 94*, 9085−9090.
36. Ädelroth, P., Ek, M. S., Mitchell, D. M., Gennis, R. B., and Brzezinski, P. (1997) Glutamate 286 in cytochrome aa_3 from *Rhodobacter sphaeroides* is involved in proton uptake during the reaction of the fully-reduced enzyme with dioxygen, *Biochemistry 36*, 13824−13829.
37. Brzezinski, P., and Ädelroth, P. (1998) Pathways of proton transfer in cytochrome *c* oxidase, *J. Bioenerg. Biomembr. 30*, 99−107.
38. Ädelroth, P., Gennis, R. B., and Brzezinski, P. (1998) Role of the pathway through K(I-362) in proton transfer in cytochrome *c* oxidase from *R. sphaeroides*, *Biochemistry 37*, 2470−2476.
39. Zaslavsky, D., and Gennis, R. B. (1998) Substitution of lysine-362 in a putative proton-conducting channel in the cytochrome *c* oxidase from *Rhodobacter sphaeroides* blocks turnover with O_2 but not with H_2O_2, *Biochemistry 37*, 3062−3067.
40. Bränden, M., Sigurdson, H., Namslauer, A., Gennis, R. B., Ädelroth, P., and Brzezinski, P. (2001) On the role of the K-proton-transfer pathway: Cytochrome *c* oxidase, *Proc. Natl. Acad. Sci. U.S.A. 98*, 5013−5018.
41. Nicholls, P., and Singh, A. P. (1988) *Life Sci. Adv. (Agra, India) 7*, 321−326.
42. Kita, K., Kasahara, M., and Anraku, Y. (1982) Formation of a membrane potential by reconstructed liposomes made with cytochrome b_{562}-*o* complex, a terminal oxidase of *Escherichia coli* K12, *J. Biol. Chem. 257*, 7933−7935.
43. Kannt, A., Ostermann, T., Müller, H., and Ruitenberg, M. (2001) Zn^{2+} binding to the cytoplasmic side of *Paracoccus denitrificans* cytochrome *c* oxidase selectively uncouples electron transfer and proton translocation, *FEBS Lett. 503*, 142−146.
44. Mills, D. A., Schmidt, B., Hiser, C., Westley, E., and Ferguson-Miller, S. (2002) Membrane potential-controlled inhibition of cytochrome *c* oxidase by zinc, *J. Biol. Chem. 277*, 14894−14901.
45. Aagaard, A., and Brzezinski, P. (2001) Zinc ions inhibit oxidation of cytochrome *c* oxidase by oxygen, *FEBS Lett. 494*, 157−60.
46. Aagaard, A., Namslauer, A., and Brzezinski, P. (2002) Inhibition of proton transfer in cytochrome *c* oxidase by zinc ions: delayed proton uptake during oxygen reduction, *Biochim. Biophys. Acta 1555*, 133−139.
47. Paddock, M. L., Graige, M. S., Feher, G., and Okumura, M. Y. (1999) Identification of the proton pathway in bacterial reaction centers: inhibition of proton transfer by binding of Zn^{2+} or Cd^{2+}, *Proc. Natl. Acad. Sci. U.S.A. 96*, 6183−6188.
48. Ädelroth, P., Paddock, M. L., Sagle, L. B., Fehrer, G., and Okumura, M. Y. (2000) Identification of the proton pathway in bacterial reaction centers: both protons associated with reduction of Q_B to Q_BH_2 share a common entry point, *Proc. Natl. Acad. Sci. U.S.A. 97*, 13086−13091.
49. Axelrod, H. L., Abresch, E. C., Paddock, M. L., Okumura, M. Y., and Feher, G. (2000) Determination of the binding sites of the proton-transfer inhibitors Cd^{2+} and Zn^{2+} in bacterial reaction centers, *Proc. Natl. Acad. Sci. U.S.A. 97*, 1542−1547.
50. Link, T. A., and von Jagow, G. (1995) Zinc ions inhibit the Q_P center of bovine heart mitochondrial bc_1 complex by blocking a protonatable group, *J. Biol. Chem. 270*, 25001−25006.
51. Cherny, V. V., and DeCoursey, T. E. (1999) pH-dependent inhibition of voltage-gated H^+ currents in rat alveolar epithelial cells by Zn^{2+} and other divalent cations, *J. Gen. Physiol. 114*, 819−838.
52. Van Eps, N., Szundi, I., and Einarsdóttir, Ó. (2003) pH dependence of the reduction of dioxygen to water by cytochrome *c* oxidase. 1. The P_R state is a pH-dependent mixture of three intermediates, A, P, and F, *Biochemistry 42*, 5065−5073.
53. Szundi, I., Van Eps, N., and Einarsdóttir, Ó. (2003) pH dependence of the reduction of dioxygen to water by cytochrome *c* oxidase. 2. Branched electron-transfer pathways linked by proton transfer, *Biochemistry 42*, 5074−5090.
54. Einarsdóttir, Ó., Szundi, I., Van Eps, N., and Sucheta, A. S. (2002) P_M and P_R forms of cytochrome *c* oxidase have different spectral properties, *J. Inorg. Biochem. 91*, 87−93.
55. Yoshikawa, S., Choc, M. G., O'Toole, M. C., and Caughey, W. S. (1977) An infrared study of CO binding to heart cytochrome *c* oxidase and hemoglobin A, *J. Biol. Chem. 252*, 5498−5508.
56. Antalis, T. M., and Palmer, G. (1982) Kinetic characterization of the interaction between cytochrome oxidase and cytochrome *c*, *J. Biol. Chem. 257*, 6194−6206.
57. Gibson, Q. H., and Greenwood, C. (1963) Reactions of cytochrome oxidase with oxygen and carbon monoxide, *Biochem. J. 86*, 541−554.
58. Greenwood, C., and Gibson, Q. H. (1967) The reaction of reduced cytochrome *c* oxidase with oxygen, *J. Biol. Chem. 242*, 1782−1787.
59. Szundi, I., Liao, G.-L., and Einarsdóttir, Ó. (2001) Near-infrared time-resolved optical absorption studies of the reaction of fully reduced cytochrome *c* oxidase with dioxygen, *Biochemistry 40*, 2332−2339.
60. Slutter, C. E., Sanders, D., Wittung, P., Malmström, B. G., Aasa, R., Richards, J. H., Gray, H. B., and Fee, J. A. (1996) Water-soluble recombinant Cu_A-domain of the cytochrome ba_3 from subunit II from *Thermus thermophilus*, *Biochemistry 35*, 3387−3395.

61. Fabian, M., and Palmer, G. (1995) The interaction of cytochrome oxidase with hydrogen peroxide: The relationship of compounds P and F, *Biochemistry 34*, 13802−13810.
62. Ädelroth, P., Ek, M., and Brzezinski, P. (1998) Factors determining electron-tansfer rates in cytochrome *c* oxidase: investigation of the oxygen reaction in the *R. sphaeroides* enzyme, *Biochim. Biophys. Acta 1367*, 107−117.
63. Morgan, J. E., Li, P. M., Jang, D.-J., El-Sayed, M. A., and Chan, S. I. (1989) Electron transfer between cytochrome *a* and copper A in cytochrome *c* oxidase: A perturbed equilibrium study, *Biochemistry 28*, 6975−6983.
64. Oliveberg, M., and Malmström, B. G. (1991) Internal electron transfer in cytochrome *c* oxidase: Evidence for a rapid equilibrium between cytochrome *a* and the bimetallic site, *Biochemistry 30*, 7053−7057.
65. Verkhovsky, M. I., Morgan, J. E., and Wikström, M. (1992) Intramolecular electron transfer in cytochrome *c* oxidase: A cascade of equilibria, *Biochemistry 31*, 11860−11863.
66. Georgiadis, K. E., Jhon, N.-I., and Einarsdóttir, Ó. (1994) Time-resolved optical absorption studies of intramolecular electron transfer in cytochrome *c* oxidase, *Biochemistry 33*, 9245−9256.
67. Einarsdóttir, Ó., Georgiadis, K. E., and Sucheta, A. (1995) Intramolecular electron transfer and conformational changes in cytochrome *c* oxidase, *Biochemistry 34*, 496−508.
68. Han, S., Ching, Y.-C., and Rousseau, D. L. (1990) Cytochrome *c* oxidase: Decay of the primary oxygen intermediate involves direct electron transfer from cytochrome *a*, *Proc. Natl. Acad. Sci. U.S.A. 87*, 8408−8412.
69. Hill, B. C., Greenwood, C., and Nicholls, P. (1986) Intermediate steps in the reaction of cytochrome oxidase with molecular oxygen, *Biochim. Biophys. Acta 853*, 91−113.
70. Sucheta, A., Georgiadis, K. E., and Einarsdóttir, Ó. (1997) Mechanism of cytochrome *c* oxidase-catalyzed reduction of dioxygen to water. Evidence for peroxy and ferryl intermediates at room temperature, *Biochemistry 36*, 554−565.
71. Karpefors, M., Ädelroth, P., Zhen, Y., Ferguson-Miller, S., and Brzezinski, P. (1998) Proton uptake controls electron transfer in cytochrome *c* oxidase, *Proc. Natl. Acad. Sci. U.S.A. 95*, 13606−13611.
72. Konstantinov, A. A. (1998) Cytochrome *c* oxidase as a proton-pumping peroxidase: reaction cycle and electrogenic mechanism, *J. Bioenerg. Biomembr. 30*, 121−130.
73. Jasaitis, A., Verkhovsky, M. I., Morgan, J. E., Verkhovskaya, M. L., and Wikström, M. (1999) Assignment and charge translocation stoichiometries of the major electrogenic phases in the reaction of cytochrome *c* oxidase with dioxygen, *Biochemistry 38*, 2697−2706.
74. Verkhovsky, M. I., Jasaitis, A., Verkhovskaya, M. L., Morgan, J. E., and Wikström, M. (1999) Proton translocation by cytochrome *c* oxidase, *Nature 400*, 480−483.
75. Michel, H. (1998) The mechanism of proton pumping by cytochrome *c* oxidase, *Proc. Natl. Acad. Sci. U.S.A. 95*, 12819−12824.
76. Wikström, M., and Verkhovsky, M. I. (2002) Proton translocation by cytochrome *c* oxidase in different phases of the catalytic cycle, *Biochim. Biophys. Acta 1555*, 128−132.
77. Bränden, M., Namslauer, A., Hansson, Ö., Aasa, R., and Brzezinski, P. (2003) Water-hydroxide exchange reactions at the catalytic site of heme-copper oxidases, *Biochemistry 42*, 13178−13184.
78. Brittain, T., Little, R. H., Greenwood, C., and Watmough, N. J. (1996) The reaction of *Escherichia coli* cytochrome *bo* with H_2O_2: Evidence for the formation of an oxyferryl species by two distinct routes, *FEBS Lett. 399*, 21−25.
79. Jünemann, S., Heathcote, P., and Rich, P. R. (2000) The reactions of hydrogen peroxide with bovine cytochrome *c* oxidase, *Biochim. Biophys. Acta 1456*, 56−66.
80. Pecoraro, C., Gennis, R. B., Vygodina, T. V., and Konstantinov, A. A. (2001) Role of the K-channel in the pH-dependence of the reaction of cytochrome *c* oxidase with hydrogen peroxide, *Biochemistry 40*, 9695−9708.

BI049408P